

# A Framework for Supervised and Unsupervised Segmentation and Classification of Materials Microstructure Images

Kungang Zhang<sup>1</sup>

Daniel W. Apley<sup>1</sup>

Wei Chen<sup>2</sup>

Wing K. Liu<sup>2</sup>

L. Catherine Brinson<sup>3</sup>

<sup>1</sup>Department of Industrial Engineering and Management Sciences,  
Northwestern University

<sup>2</sup>Department of Mechanical Engineering,  
Northwestern University

<sup>3</sup>Department of Mechanical Engineering & Materials Science,  
Duke University

February 12, 2025

## Abstract

Microstructure of materials is often characterized through image analysis to understand processing-structure-properties linkages. We propose a largely automated framework that integrates unsupervised and supervised learning methods to classify micrographs according to microstructure phase/class and, for multiphase microstructures, segments them into different homogeneous regions. With the advance of manufacturing and imaging techniques, the ultra-high resolution of imaging that reveals the complexity of microstructures and the rapidly increasing quantity of images (i.e., micrographs) enables and necessitates a more powerful and automated framework to extract materials characteristics and knowledge. The framework we propose can be used to gradually build a database of microstructure classes relevant to a particular process or group of materials, which can help in analyzing and discovering/identifying new materials. The framework has three steps: (1) segmentation of multiphase micrographs through a recently developed score-based method so that different microstructure homogeneous regions can be identified in an unsupervised

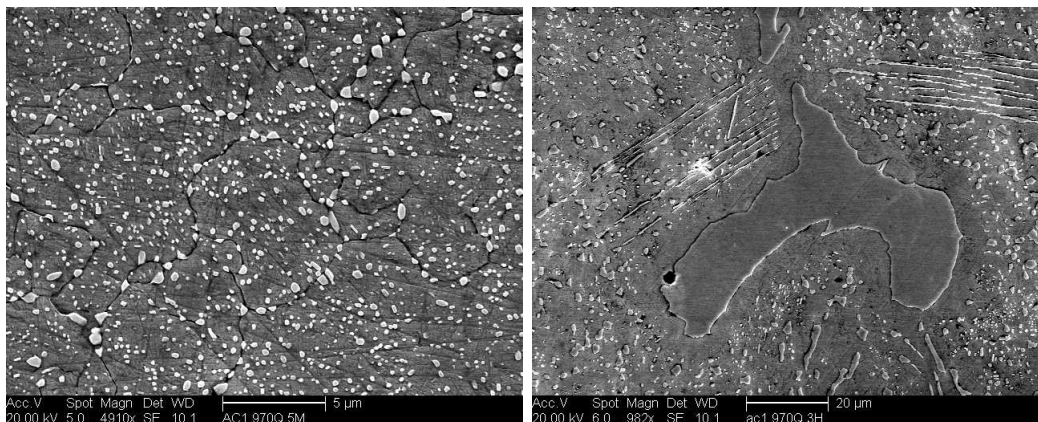
manner; (2) identification and classification of homogeneous regions of micrographs through an uncertainty-aware supervised classification network trained using the segmented micrographs from Step 1 with their identified labels verified via the built-in uncertainty quantification and minimal human inspection; (3) supervised segmentation (more powerful than the segmentation in Step 1) of multiphase microstructures through a segmentation network trained with micrographs and the results from Steps 1-2 using a form of data augmentation. This framework can iteratively characterize/segment new homogeneous or multiphase materials while expanding the database to enhance performance. The framework is demonstrated on various sets of materials and texture images.

*Keywords:* Microstructure, Fisher Score Vector, Evidential Deep Learning, Segmentation Network, Data Augmentation

# 1 Motivation and Introduction

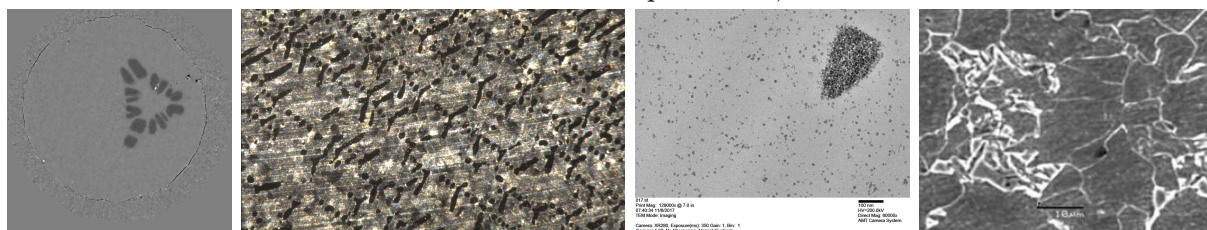
Microstructure plays a vital role in determining physical properties of materials and understanding the relations among the processes, structures, and properties DeCost and Holm (2015). Recently, analyzing images of multiphase materials, often called micrographs O’Mara et al. (2016); Puchala et al. (2016); Michel and Meredig (2016), has attracted much attention across different materials fields (e.g., metals Lewandowski and Seifi (2016), polymer composites Ligon et al. (2017), and ceramics Chen et al. (2019b); Moritz and Maleksaeedi (2018), etc.) due to burgeoning manufacturing and imaging techniques Balla et al. (2012); Bandyopadhyay and Heer (2018). For example, the ultra-high carbon steel (UHCS) data set DeCost et al. (2017b) includes 961 SEM micrographs, of which two multiphase microstructures are shown in Fig. 1a and 1b. Fig. 1a is a micrograph containing a single spheroidite phase, while Fig. 1b contains ferritic, proeutectoid, spheroidite, and Widmanstätten phases. Because the phase characteristics impact material properties (e.g., toughness and crack initiation etc.) Hecht et al. (2016); Carter et al. (2014), identifying and classifying the individual phases present in a micrograph is an important step towards understanding the physical properties of the material. Throughout this paper, by “multiphase” we mean a microstructure whose stochastic nature (different phases have different stochastic nature) varies spatially, sometimes referred to as microstructure nonstationarity. This includes certain steels that have different phases present simultaneously by design, as well as certain composites whose stochastic microstructure composition varies spatially due to variation in the processing conditions. By “single-phase”, we mean a homogeneous microstructure whose stochastic nature is spatially stationary. Throughout the paper, the

term “microstructure class” (MC) refers to the label assigned to each homogeneous region (HR) of connected pixels within a micrograph with each HR comprised of a single phase.



(a) An SEM image of UHCS with single spheroidite phase.

(b) An SEM micrograph of UHCS with multiphase: ferritic, proeutectoid, spheroidite, and Widmanstätten.



(c) Al-Zn alloy.

(d) Pb-Sn alloy.

(e) Silica in PMMA.

(f) Dual-phase steel.

Figure 1: Examples of single phase (a) and multiphase materials (b)-(f)<sup>0</sup>. (a)-(b) Two SEM images of the UHCS data set DeCost et al. (2017b); Hecht et al. (2016). Notice that the two images are not in the same magnification, a commonly encountered issue of data quality in real data sets. (c) A X-ray CT (XCT) image of dendrite growth from a solidification experiment on a Al-Zn alloy Stan et al. (2020). (d) A serial sectioning (SS) image of dendrite growth from a coarsening experiment on a Pb-Sn alloy Stan et al. (2020). (e) A TEM image of silica particles in PMMA. (f) An SEM image of dual-phase steel Banerjee et al. (2013).

The primary purpose of this paper is to introduce a framework for segmenting each micrograph into HRs/phases and classifying each HR as either an existing MC from a database of previously-identified MCs or a new MC. As new MCs are identified in our framework, they are added to the database. This framework is versatile in a sense that it

<sup>0</sup>Original micrographs with ultra-high resolution can be found through links in DeCost et al. (2017b).

can be applied to micrographs collected by different instruments (e.g., SEM, TEM, X-ray CT, Optical Microscopy, etc. Puchala et al. (2016); Gagliardi (2015); Takahashi and Tanaka (2016); Blaiszik et al. (2016); Jain et al. (2016a,b); Kim et al. (2016); Rose et al. (2017); AFRL (2018)) for various materials (e.g., metals Lewandowski and Seifi (2016), polymer composites Ligon et al. (2017), and ceramics Chen et al. (2019b); Moritz and Maleksaeedi (2018), etc.) across many industrial applications (e.g., additive manufacturing Balla et al. (2012); Bandyopadhyay and Heer (2018), quality control Bui and Apley (2018)).

Characterizing material microstructures has long been a major research focus. Recently, machine learning (ML), deep learning (DL), and AI have received growing interest in this area Stan et al. (2020); Maik Jablonka et al. (2020); Ajioka et al. (2020); Agrawal and Choudhary (2019). These approaches transform traditional methods of characterization, enabling data-driven Processing-Structure-Properties-Performance (PSP) linkages Agrawal and Choudhary (2016). Traditionally, methods for pre-processing (for many downstream tasks) and analyzing multiphase micrographs were largely manual or semi-automated. For example, some methods rely on handcrafted descriptors (e.g., volume fraction, dispersion) Ashby and Cebon (1993); Xu et al. (2014). Though intuitively appealing and sometimes effective, they are not generic to materials and fail to fully represent and distinguish complex morphologies Kondo et al. (2017). Statistical encoders (e.g., N-point correlation functions) can better represent microstructures but are often computationally expensive, depend on prior knowledge, and are limited in characterizing complex patterns in generic materials microstructures DeCost and Holm (2015); Yabansu et al. (2017); Xu et al. (2015); Yu et al. (2017). The rich micrograph data sources that are now available war-

rant more automated methods that take advantage of modern machine learning algorithms. ML/DL can learn features directly from raw images. For instance, convolutional neural networks (CNNs) eliminate manual feature extraction and have achieved high accuracy in segmentation, phase identification, and particle size estimation DeCost et al. (2019); Jang et al. (2019); DeCost et al. (2017a). Even though many machine learning methods have been effectively applied to materials science problems, including micrograph segmentation, there remain challenges in expanding this interdisciplinary research: Much of the existing work centers on supervised learning that requires a large amount of labeled data (e.g., micrographs labeled pixel-by-pixel according to their microstructure class) Kondo et al. (2017); Lubbers et al. (2017); Azimi et al. (2018); Strohmam et al. (2019); Chen et al. (2019a) to train a segmentation model to reach a high accuracy. Moreover, works utilizing unsupervised or semi-supervised learning methods usually do not require labels during training Liu et al. (2024); Zhang et al. (2023); Huang et al. (2023) but still need manual identification and/or classification and are more expensive and less powerful than their supervised counterparts in production DeCost et al. (2017a); Impoco and Tuminello (2015); Kitahara and Holm (2018); Zhang et al. (2021). This study proposes a hybrid framework combining aspects of both approaches. By leveraging minimal labels and iterative refinement, we aim to produce accurate, scalable, and efficient microstructure characterization. In Section 2, we discuss the theoretical foundations and methods for each step of our framework. In Section 3, data sets, demonstrations, and experiment results for each step are presented, demonstrating that our approach can enhance characterization tasks with minimal human intervention.

## 2 Theoretical Foundation and Methodology

To address the motivations and challenges discussed in the introduction, we propose a framework for characterizing single-phase or multiphase microstructures with the following major steps and advantages (also see the flow chart in Fig. 2):

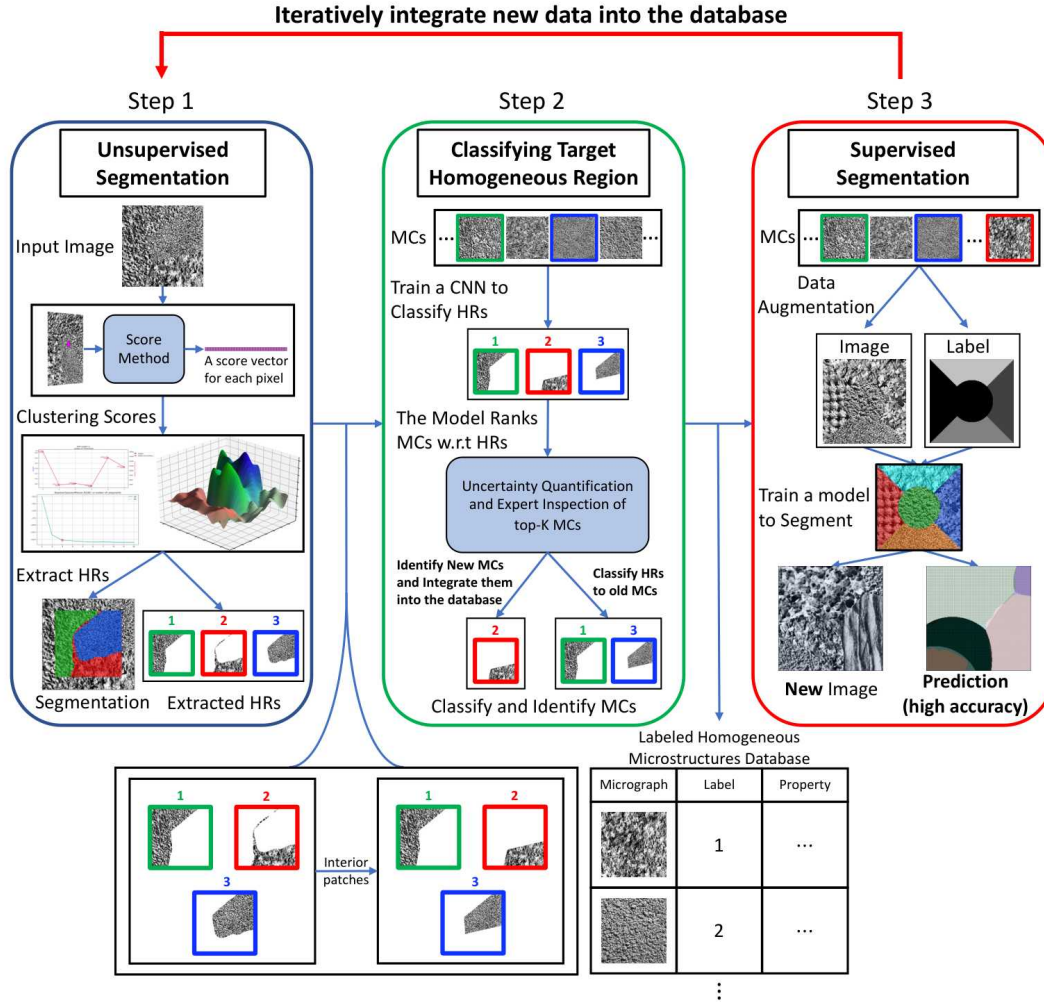


Figure 2: Flow chart of the iterative framework. Between steps, the knowledge passed from the previous to the next are shown: from Step 1 to 2, the HRs are extracted and entered into the database of existing MCS; from Step 2 to 3, the database of classified and labeled homogeneous microstructures is passed for data augmentation and training segmentation networks.

**Step 1:** *In an unsupervised manner, characterize multiphase nonstationary behavior in*

micrographs using a recently developed score-based nonstationarity analysis method Zhang et al. (2021) (see Sec. 2.1). Specifically, we fit a single supervised learning model to a set of training micrograph(s) to predict the grayscale value for each pixel, as a function of some window of neighboring pixels, which provides a fingerprint to the stochastic nature of the microstructure. We then apply the model to predict each pixel of the training micrograph(s) to obtain score vectors (see Eq. (1) later) pixel-by-pixel, and then cluster score vectors to segment HRs corresponding to distinct MCs. Note that our use of supervised learning in this step differs from existing supervised learning approaches in which the supervised learning model is a classification model to classify MC at each pixel, which requires MC labels to train.

**Step 2:** The extracted HRs from Step 1 are either classified as one of the previously identified and analyzed MCs in the database or, based on our classification uncertainty quantification, determined to be a new MC not previously cataloged. To do this, an uncertainty-aware model predicts which existing MC a target HR belongs to and ranks the different MCs based on similarity to the target HR along with an uncertainty measure of the confidence of the prediction. If the target HR has high uncertainty it is concluded to be different from any existing MC (which can be verified with minimal human inspection), and the new MC is integrated into the database and the classification model. This largely shifts the burden of screening/memorizing morphologies and patterns of an entire database of MCs from humans to algorithms and thus accelerates discovery/identification of new materials.

**Step 3:** The database of MCs and their corresponding labels are then used to train a supervised segmentation model through data augmentation to improve segmentation quality



*relative to the segmentation in Step 1. This provides more automated, more accurate, and faster identification, classification, and segmentation of MCs for potential use for in-situ monitoring and real-time control of production/processing.*

**Iteration over Steps 1-3:** *As new micrographs are collected, they pass through the above three steps to classify/segment their phases and label any new, previously unseen, phases as new MCs (as in Step 2) and to provide additional samples of existing MCs. The iterations are intended to improve the data-driven models (e.g., classification or segmentation neural networks) by either increasing the number of MCs they can classify (if one of the phases is labeled as a new MC) or by further training the models on the newly acquired additional samples of existing MCs.*

As described in the Introduction, our iterative framework integrates supervised and unsupervised learning in a way that combines the strengths of these two types of existing approaches for micrograph segmentation and classification. In the remainder of this section, we describe the details of each step of the framework.

## **2.1 Step 1: Micrograph nonstationarity analysis and unsupervised segmentation**

In general, the microstructure of materials can be modeled as realizations of a spatial random process in the following manner. Denote the concatenated  $m$  pixel values in a micrograph as a vector  $\mathbf{X} = [X_1, X_2, \dots, X_m]$ . The value at the  $i^{\text{th}}$  pixel, conditioned on all other pixels in the micrograph, can be seen as a random variable  $X_i$  drawn from a conditional distribution that is approximated as  $P(X_i|\mathbb{N}(X_i))$ , where  $\mathbb{N}(X_i)$  denotes some

local neighborhood of pixel values surrounding the  $i^{\text{th}}$  pixel as shown in Fig. 3a Bostanabad et al. (2016). Via Gibbs sampling arguments, this conditional distribution  $P(X_i|\mathbb{N}(X_i))$  can be viewed as characterizing the joint distribution of all pixels in the micrograph and, thus, the stochastic nature of the microstructure.

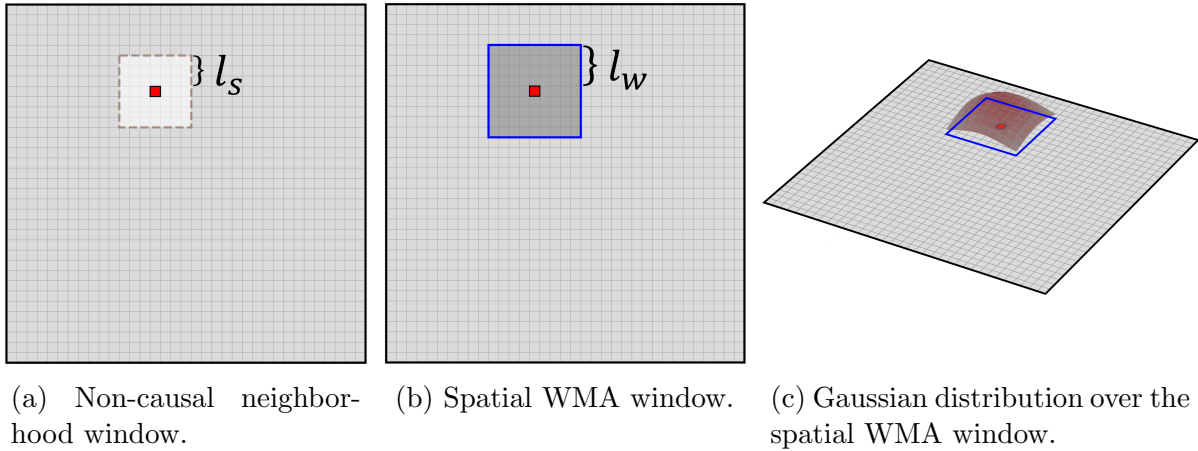


Figure 3: Illustration of processing score vectors. (a) Neighborhood window (brown dashed square excluding the target pixel colored as red) for modeling the conditional distribution of  $X_i$  (the red pixel) given the neighboring pixels in the window. (b) Spatial WMA window (blue square including the target pixel colored as red) for spatially smoothing score vectors. (c) A 2D Gaussian weighting function is centered (at the red pixel) and truncated over the WMA window. The height of profile and grayscale value is proportional to the density value of the weighting function.

Any appropriate supervised learning model (e.g., a neural network) can be fit to all the observations  $\{(X_i, \mathbb{N}(X_i))\}_{i=1}^m$  (with  $X_i$  and  $\mathbb{N}(X_i)$  being the response and the predictor variables, respectively) from a training micrograph(s), as a means of modeling the distribution  $P(X|\mathbb{N}(X); \boldsymbol{\theta})$  with model parameters denoted by  $\boldsymbol{\theta}$  (e.g., the weights for all neurons in a neural network).  $\boldsymbol{\theta}$  implicitly represents the distribution of the pixels in the micrograph and therefore provides a relatively compact “fingerprint” that represents the stochastic nature of the microstructure. We adopt the approach developed in Zhang et al. (2021) for monitoring for nonstationarity in the nature of the microstructure using Fisher

score vectors, which, for the  $i^{\text{th}}$  pixel, is defined as

$$\mathbf{s}(\boldsymbol{\theta}; y_i, \mathbf{x}_i) = \nabla_{\boldsymbol{\theta}} \log P(X = y_i | \mathbb{N}(X) = \mathbf{x}_i; \boldsymbol{\theta}) \quad (1)$$

where  $\nabla_{\boldsymbol{\theta}}$  is the gradient operator with respect to  $\boldsymbol{\theta}$ ;  $y_i$  and  $\mathbf{x}_i$  are the observations of the  $i^{\text{th}}$  pixel and the vector of pixels over its chosen local neighborhood. For grayscale images, the conditional distribution of  $X$  given  $\mathbb{N}(X) = \mathbf{x}$  is approximated as normal with mean  $g(\mathbf{x}; \boldsymbol{\theta})$  and variance  $\sigma^2$ , where  $g(\mathbf{x}; \boldsymbol{\theta})$  is the prediction of  $X$  from the supervised learning model. Under mild conditions, if the microstructure is stationary over the region associated with the training data and the supervised learning model is “correct”, the score vector is zero-mean in the sense that

$$E_{\boldsymbol{\theta}}[\mathbf{s}(\boldsymbol{\theta}; X, \mathbb{N}(X))] = \mathbf{0} \quad (2)$$

where  $E_{\boldsymbol{\theta}}[\cdot]$  denotes the expectation operator (with respect to the random variables  $X$  and  $\mathbb{N}(X)$ ), and the subscript  $\boldsymbol{\theta}$  indicates that the distribution of pixel value  $X$  and its neighborhood values  $\mathbb{N}(X)$  are based on the supervised learning model with true parameters  $\boldsymbol{\theta}$ . Conversely, if the local stochastic nature in the vicinity of pixel  $X$  changes from what it was over the training data (i.e., the true parameters change from  $\boldsymbol{\theta}$  to  $\boldsymbol{\theta}' \neq \boldsymbol{\theta}$  at  $X$ ), then the mean of the score vector at  $X$  for a model with parameters  $\boldsymbol{\theta}$  generally differs from zero (i.e.,  $E_{\boldsymbol{\theta}'}[\mathbf{s}(\boldsymbol{\theta}; X, \mathbb{N}(X))] \neq \mathbf{0}$ ). In practice,  $\boldsymbol{\theta}$  for the training data is replaced by its maximum likelihood estimate  $\hat{\boldsymbol{\theta}}$ , and the expectation in Eq. (2) is replaced by the empirical mean  $\hat{E}_{\boldsymbol{\theta}}[\mathbf{s}(\hat{\boldsymbol{\theta}}; X, \mathbb{N}(X))]$  over all pixels in the micrograph training data (for details refer

to Zhang et al. (2021)). Here, the subscript  $\theta$  indicates whatever parameters are valid in the vicinity of pixel  $X$ , and  $\hat{\theta}$  indicates the globally estimated parameters over the training data.

From the preceding arguments, the problem of analyzing nonstationarity in the microstructure over a micrograph(s) is converted to fitting a single supervised learning model to the micrograph(s), applying the model to predict each pixel, and then analyzing whether the mean score vector locally differs substantially from the zero vector anywhere in the micrograph(s). If the stochastic nature of different MCs, as captured by  $\theta$ , is distinct enough, the score vectors belonging to different HRs should center around different mean vectors and be separable in the score-vector space. Thus, a clustering algorithm can be applied to the (smoothed version of, via some spatial moving window) score vectors  $\mathbf{s}(\hat{\theta}; y_i, \mathbf{x}_i)$  to diagnose the spatial nonstationarity of micrographs or, more specifically, segment different HRs based on their stochastic natures in an unsupervised manner Zhang et al. (2021). To mitigate the effects of noise in the score vectors on the clustering performance, before clustering, we calculate a spatial Gaussian weighted moving average (WMA) of score vectors, denoted as  $\mathbf{z}_i$  for the  $i^{\text{th}}$  pixel, where the WMA window and the 2D weight density functions are depicted in Fig. 3b and 3c.

To cluster score vectors and segment the micrograph into HRs, we use the Bayesian Gaussian Mixture (BGM) clustering method Bishop (2006). Within the clustering algorithm, the number of clusters (corresponding to the number of HRs) must be estimated. For this we use AIC/BIC curves and posterior weights plot produced within the BGM clustering algorithm. We focus on the BGM approach, which is a more computationally

expensive clustering method than the basic *k-means* clustering method, because it provides more information on the number of clusters. More specifically, we use the following Bayesian Gaussian mixture model for the smoothed version of the score vectors  $\mathbf{z}_i$  with their latent class one-hot encoding labels  $\mathbf{c}_i$ :

$$\begin{aligned}
& p(\{\mathbf{z}_i\}_{i=1}^m, \{\mathbf{c}_i\}_{i=1}^m, \boldsymbol{\pi}, \boldsymbol{\mu}, \boldsymbol{\Lambda}) \\
&= \prod_{i=1}^m p(\mathbf{z}_i | \mathbf{c}_i, \boldsymbol{\mu}, \boldsymbol{\Lambda}) p(\mathbf{c}_i | \boldsymbol{\pi}) p(\boldsymbol{\pi}) p(\boldsymbol{\mu}, \boldsymbol{\Lambda}) \\
&= \prod_{i=1}^m \prod_{k=1}^K \mathcal{N}(\mathbf{z}_i | \boldsymbol{\mu}_k, \boldsymbol{\Lambda}_k^{-1})^{c_{i,k}} \pi_k^{c_{i,k}} p(\boldsymbol{\pi}) p(\boldsymbol{\mu}, \boldsymbol{\Lambda}) \tag{3}
\end{aligned}$$

where  $\boldsymbol{\pi} = [\pi_1, \pi_2, \dots, \pi_K]$  is the mixing proportion of each cluster;  $\boldsymbol{\mu} = \{\boldsymbol{\mu}_k\}_{k=1}^K$  and  $\boldsymbol{\Lambda} = \{\boldsymbol{\Lambda}_k\}_{k=1}^K$  are the mean vectors and precision matrices of Gaussian distribution associated with each cluster, respectively; and  $\mathbf{c}_i = [c_{i,1}, c_{i,2}, \dots,$

$c_{i,K}]$  is the standard one-hot encoding vector of zeros with a one in the  $k^{\text{th}}$  position if  $\mathbf{z}_i$  is in

cluster  $k$ . The last equation above utilizes the relations  $p(\mathbf{z}_i | \mathbf{c}_i, \boldsymbol{\mu}, \boldsymbol{\Lambda}) = \prod_{k=1}^K \mathcal{N}(\mathbf{z}_i | \boldsymbol{\mu}_k, \boldsymbol{\Lambda}_k^{-1})^{c_{i,k}}$

and  $p(\mathbf{c}_i | \boldsymbol{\pi}) = \prod_{k=1}^K \pi_k^{c_{i,k}}$ . The prior distributions of parameters  $\boldsymbol{\pi}$ ,  $\boldsymbol{\mu}$ , and  $\boldsymbol{\Lambda}$  are:

$$p(\boldsymbol{\pi}) = \text{Dir}(\boldsymbol{\pi} | \boldsymbol{\alpha}_0) \tag{4}$$

$$p(\boldsymbol{\mu}, \boldsymbol{\Lambda}) = \prod_{k=1}^K \mathcal{N}(\boldsymbol{\mu}_k | \boldsymbol{\mu}_0, (\beta_0 \boldsymbol{\Lambda}_k)^{-1}) \text{Wishart}(\boldsymbol{\Lambda}_k | \mathbf{W}_0, \nu_0) \tag{5}$$

where  $\text{Dir}(\boldsymbol{\pi} | \boldsymbol{\alpha}_0)$  is the Dirichlet distribution with parameter vector  $\boldsymbol{\alpha}_0$ ;

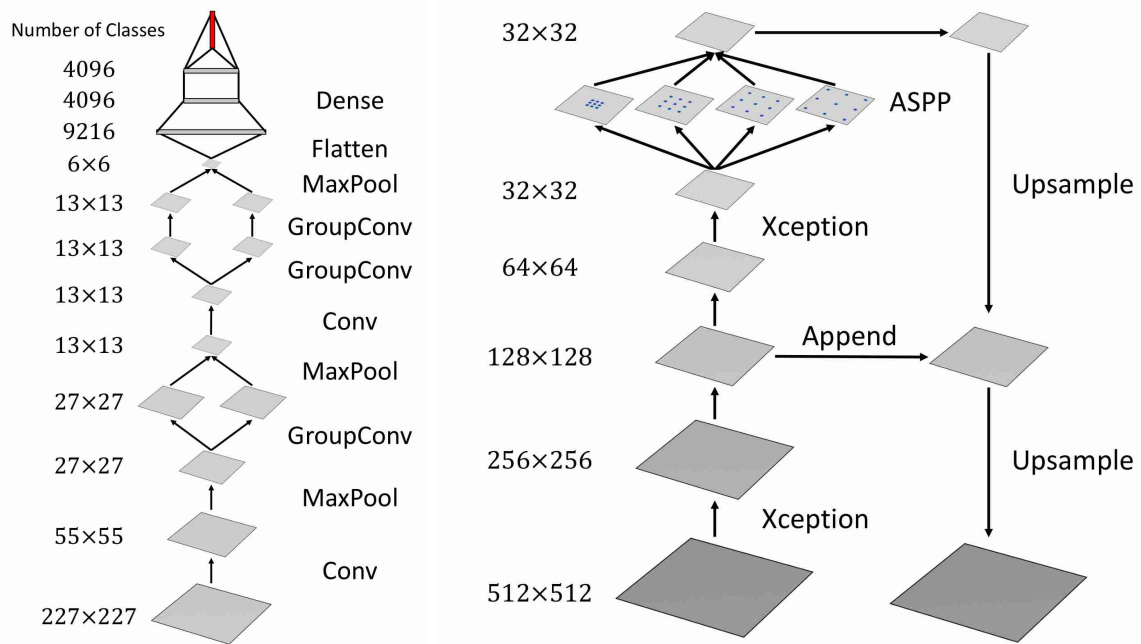
$\mathcal{N}(\boldsymbol{\mu}_k | \boldsymbol{\mu}_0, (\beta_0 \boldsymbol{\Lambda}_k)^{-1})$  is the multivariate Gaussian distribution with mean vector  $\boldsymbol{\mu}_0$  and

precision matrix  $\beta_0 \mathbf{\Lambda}_k$ ; and  $\text{Wishart}(\mathbf{\Lambda}_k | \mathbf{W}_0, \nu_0)$  is the Wishart distribution with scale matrix  $\mathbf{W}_0$  and degrees of freedom  $\nu_0$ . We follow standard rules Bishop (2006); Blei et al. (2003); Teh et al. (2004) for choice of all hyperparameters  $\boldsymbol{\alpha}_0$ ,  $\boldsymbol{\mu}_0$ ,  $\beta_0$ ,  $\mathbf{W}_0$ , and  $\nu_0$ . In particular, we use  $\alpha_{0,k} = 10^{-9} (k = 1, 2, \dots, K)$ ,  $\boldsymbol{\mu}_0 = \frac{1}{m} \sum_{i=1}^m \mathbf{z}_i$ ,  $\beta_0 = 1$ ,  $\mathbf{W}_0^{-1} = \frac{1}{m-1} \sum_{i=1}^m (\mathbf{z}_i - \bar{\mathbf{z}})(\mathbf{z}_i - \bar{\mathbf{z}})^T$ , and  $\nu_0 = \text{dim}(\mathbf{z}_i)$ . We then use the standard variational inference algorithm to compute posterior distributions for parameters  $\boldsymbol{\pi}$ ,  $\{\boldsymbol{\mu}_k\}_{k=1}^K$ , and  $\{\mathbf{\Lambda}_k\}_{k=1}^K$  and latent variables  $\{\mathbf{c}_i\}_{i=1}^m$  and use their maximum a posteriori estimators as point estimates. The posterior estimate of the mixing proportion  $\boldsymbol{\pi}$  can be used to determine the number of clusters in the micrograph, because the  $k^{\text{th}}$  element  $\pi_k$  can be thought of as the portion of the effective number of  $\mathbf{z}_i$ 's assigned to the  $k^{\text{th}}$  cluster. This is a key feature of BGM that can help determine the number of clusters in a data-driven manner. See the later examples (e.g., Fig. 5c and 5d) for use of BGM posterior weights and AIC/BIC to determine the number of clusters. After estimating the number of clusters and clustering the score vectors based on the posterior distribution of  $\{\mathbf{c}_i\}_{i=1}^m$ , (each cluster represents a different MC) HRs can be obtained, possibly with minimal guidance from human experts to verify the unsupervised segmentation of HRs.

Note that over a region near the micrograph borders with width  $l_s + l_w$  ( $l_s$  and  $l_w$  are the two window half-lengths in Fig. 3a and 3b), the pixels within this border region have no smoothed score vectors due to the lack of neighboring pixels and therefore cannot be segmented in Step 1 (Fig. 6). Step 3 (Sec. 2.3) avoids this limitation and can classify the MC in the region near borders by training a supervised segmentation model incorporating the MCs and verified labels from Steps 1-2.

## 2.2 Step 2: Classification and ranking of MCs in the database using a CNN

After the unsupervised segmentation of Step 1, square patches of certain dimension cut from each of the resulting HRs (one corresponding to each identified cluster/segment) is input to a classification model to either determine which MC from the database it corresponds to or to classify it as a new MC to be added to the database. For this we train a form of CNN to automatically classify HRs according to their MCs and identify novel MCs that have not been characterized before.



(a) AlexNet architecture. The group convolutional layer breaks a feature bank into two so that they can fit into multiple GPUs.

(b) DeepLabv3+ architecture. The ASPP uses different dilation rates parallelly in filter banks to change the field-of-view of filters, so that multi-scale information is extracted simultaneously, as depicted by the blue dots with different spaces representing multiscale configurations of pixels in the ASPP layer.

Figure 4: Architectures of two Deep Learning neural networks used in Section 2.2 and Section 2.3.

We use an AlexNet CNN network Krizhevsky et al. (2012) (Fig. 4a) having five convolutional layers, some of which are followed by max-pooling layers or normalization layers, and three fully-connected layers, with a total of roughly 60 million parameters and 650 thousands neurons.

The classification network gives three outcomes simultaneously for each square patch of HR that is input to it: i) a single classified MC for each HR segment, ii) ranking of each MC within the database reflecting its similarity to the target MC of the input HR, and iii) providing an uncertainty quantification as a metric to evaluate whether the MC is a new MC not contained in the existing database. This is depicted as Step 2 in Fig. 2. This supervised CNN model facilitates efficient integration of MC labels verified by human experts into the database and the classification model. For this, the model outputs some user-specified small number  $K'$  (e.g.,  $K' = 10$ ) of MCs that are most similar to the target HR (i.e., have the highest classification probability) while the remaining MCs in the database with lower classification probabilities are automatically screened out. As part of this process, we use evidential deep learning (EDL) Sensoy et al. (2018) to also produce an uncertainty quantification that reflects the likelihood that the HR is a new MC not belonging to the existing database. If the uncertainty is high, an expert can then inspect micrographs for the input HR and  $K'$  most similar MCs, along with their classification probabilities and uncertainty quantification, to determine the ground truth and label the HR accordingly.

In EDL, instead of directly modeling the probability mass function (pmf) that the label of an input image follows (the number of possible labels is the number of MCs in the database), the neural network treats the pmf as a random vector that follows a Dirichlet



distribution. The output of the neural network in EDL is thus the vector of parameters of this Dirichlet distribution, which provides not only a mean but also uncertainty estimation of prediction. More specifically, in EDL the class pmf  $\mathbf{p}$  is assumed to follow the distribution:

$$\text{Dir}(\mathbf{p}|\boldsymbol{\alpha}) = \frac{1}{B(\boldsymbol{\alpha})} \prod_{k=1}^K p_k^{\alpha_k - 1} \quad (6)$$

where  $\sum_{k=1}^K p_k = 1$ ,  $\boldsymbol{\alpha} = [\alpha_1, \alpha_2, \dots, \alpha_K]$  are the parameters of the distribution, and  $B(\boldsymbol{\alpha})$  is the  $K$ -dimensional multinomial beta function Kotz et al. (2019). Instead of maximizing cross-entropy loss as in the usual classification neural network that only gives point estimation for class probabilities, EDL minimizes the empirical mean of the Bayes risk of a loss function for the pmf, which is defined for the  $i^{\text{th}}$  sample as:

$$\mathcal{L}(\boldsymbol{\Theta}; \mathbf{M}_i, \mathbf{t}_i) = \int L(\mathbf{p}, \mathbf{t}_i) \text{Dir}(\mathbf{p}|\boldsymbol{\alpha}_i(\mathbf{M}_i|\boldsymbol{\Theta})) d\mathbf{p} \quad (7)$$

where  $\mathbf{M}_i$  and  $\mathbf{t}_i$  are the input image and one-hot encoding label vector of the  $i^{\text{th}}$  sample, with all parameters of the neural network denoted as  $\boldsymbol{\Theta}$ . The loss function  $L(\mathbf{p}, \mathbf{t}_i)$  we used here is mean-squared-error (MSE) with exponential activation function, as recommended in Sensoy et al. (2018). The estimated class probabilities  $\hat{\mathbf{p}}_i$  and uncertainty  $\hat{u}_i$  are then calculated as  $\hat{p}_{i,k} = \alpha_{i,k} / \sum_{k=1}^K \alpha_{i,k}$  and  $\hat{u}_i = K / \sum_{k=1}^K \alpha_{i,k}$ . If an extracted HR indeed belongs to an existing MC, the uncertainty-aware classification network ideally gives low uncertainty; otherwise, the value of classification uncertainty from EDL should be high, indicating that the HR belongs to a new MC. To apply EDL, the last softmax layer of the

AlexNet is replaced with an exponential activation layer and the loss function contains the MSE loss term with Kullback-Leibler divergence penalization term.

### **2.3 Step 3: Micrograph segmentation using a supervised segmentation network**

We also use a supervised segmentation network to improve the segmentation results (relative to the initial unsupervised segmentation in Step 1) of multiphase materials, which also generates pixel-wise classification labels for MCs. The input to this segmentation network is a micrograph that could be the same micrograph input in Step 1 and the output is an image of the same spatial size as the input micrograph with each pixel replaced with the MC label to which the microstructure at that pixel belongs. This step reaches a pixel-wise accuracy higher than the unsupervised segmentation method in Step 1 and also has the capabilities of segmentation near borders of micrographs and faster segmentation of new multiphase micrographs after the model is trained. To train this model, we can either use i) data sets with full pixel-wise annotations which are usually costly; or ii) a database of homogeneous microstructures obtained in Step 2 for which pixel-wise annotations are automatically obtained and from which additional multiphase micrographs with pixel-wise annotations can be easily generated to improve the model training, as described below.

In this study, a DeepLabv3+ Chen et al. (2018) neural network is trained to segment micrographs into HRs according to their MCs. DeepLabv3+ (Fig. 4b) contains  $\sim 41$  million parameters with 293 layers and combines advantages of both the Atrous Spatial Pyramid Pooling (ASPP) and the encoder-decoder structure to encode multi-scale contextual in-

formation and capture details near boundaries between different MCs. DeepLabv3+ uses DeepLabv3 Chen et al. (2017) as the encoder, which gradually shrinks the spatial size of features and extracts higher-level information. The output of the feature extractor is usually 16 times smaller than the input size, but other shrink ratios are also possible. The decoder then gradually upsamples the learned features to the same resolution as inputs. One important part of the architecture is a skip connection, appearing in almost all popular segmentation networks (i.e., Unet Ronneberger et al. (2015), FCN Long et al. (2015), etc.): one of middle layers of the decoder is appended along the dimension of channels with the corresponding features of the same spatial size in the encoder, before being upsampled to the same size as the input images (see the arrow labeled “Append” in Fig. 4b). This skip connection also stabilizes the training and refines detailed information. In the encoder part, DeepLabv3 uses a modified Xception model Chollet (2017) and ASPP model. The Xception model was further modified Qi et al. (2017) in DeepLabv3 so that all max-pooling layers are replaced by a depthwise separable convolution (DSC) layer. The DSC layer extracts multi-scale contextual information, which is crucial for capturing MC patterns at different length-scales of an MC and also demonstrates robustness against micrograph scaling and noise. To reduce the computation cost while preserving a high segmentation accuracy, we reduce the number of some stacked components. More specifically, we reduce the number of stacked Xception layers from 20 to 8 and retain the ASPP model. The input size is reduced from  $512 \times 512$  to  $256 \times 256$ . The simplified DeepLabv3+ has only  $\sim 1.4$  million parameters, instead of the original 41 millions.

To generate multiphase micrographs for training the supervised segmentation network,

homogeneous microstructure images are randomly selected from a database like Brodatz data sets Brodatz (1966); Efros and Leung (1999); Randen and Husoy (1999) or the database from Steps 1-2 and then randomly cropped, rotated, flipped, scaled, and pasted together as depicted in Step 3 of Fig. 2. The boundaries of these micrograph patches can be either curved or straight lines to mimic realistic boundaries in micrographs. Then, these artificially generated multiphase micrographs and their labels are grouped as mini-batches to be used in the SGD algorithm to minimize the loss function (8) below. To accelerate the training process in all of our later examples, we used these generated data to pre-train the network, and then fine-tuned the training on real micrographs or the database with labels from Steps 1-2.

To train the supervised segmentation network, we use cross-entropy classification error as the loss function and account for class imbalance of different MCs. Denote a micrograph with  $m$  pixels and its pixel-wise MC labels by  $(\mathbf{X}, \mathbf{Y})$  where  $\mathbf{X} = [X_1, X_2, \dots, X_m]$  are the pixels, and  $\mathbf{Y} = [Y_1, Y_2, \dots, Y_m]$  ( $Y_i \in \{1, 2, \dots, k\}$ ), where  $k$  denotes the total number of MCs. The loss function for this micrograph is

$$l(\Theta; \mathbf{X}, \mathbf{Y}) = \sum_{i=1}^m \sum_{j=1}^k w_j^{0.5} I_{(Y_i=j)} \log p_{i,j}(\mathbf{X}; \Theta) \quad (8)$$

where  $\{w_j\}_{j=1}^k$  are class balancing weights that are inversely proportional to the frequency of each MC in the training data;  $I_{(Y_i=j)}$  is the indicator function that the true pixel label  $Y_i$  is  $j$ ;  $p_{i,j}(\mathbf{X}; \Theta)$  is the predicted probability that  $Y_i = j$ , and  $\Theta$  denotes all parameters of the segmentation network.

## 2.4 Iteration over Steps 1-3: Characterizing new micrographs and improving accuracy

Steps 1-3 can be applied to either i) a single time to a fixed set of micrographs, or ii) iteratively, to multiple sets of micrographs, when new sets are collected over time. Most existing approaches cannot be applied to the second situation, which is more consistent with the new material discovery/design process and allows previously learned information to be incorporated at each iteration to improve the computational efficiency and accuracy of the classification/segmentation. To make the learning loop more efficient, models in Steps 2 and 3 can be trained more quickly using transfer learning, as opposed to training from scratch every time micrographs of a new MC are obtained. For example, if the models are currently trained on a database of  $k$  MCs and a micrograph representing a new  $(k+1)^{\text{st}}$  MC is obtained, the training can initiate with the current network weights; then in the last layer the  $k$  output channels for the  $k$  existing classes can be appended with an additional channel with random initial weights to initiate the new training. We show later that this performs consistently better than training-from-scratch.

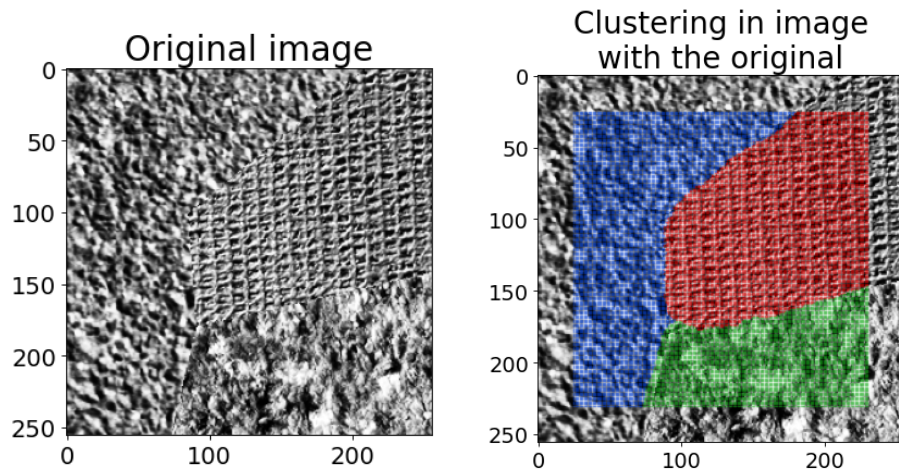
## 3 Data sets and experimental results

In this section, data sets and experiment results for Steps 1-3 are presented in order to demonstrate each step and the effectiveness of the overall framework.

### 3.1 Step 1: Unsupervised segmentation on Brodatz, PMMA, and dual-phase steel data sets

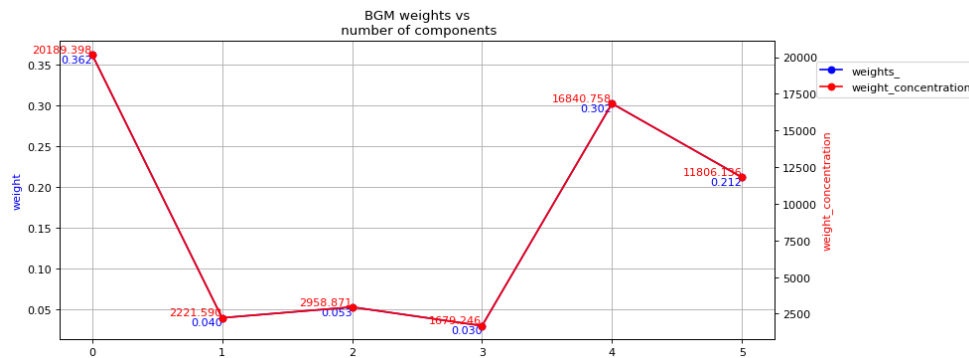
The first data set is Brodatz microstructure, an example of which is in Fig. 5. Each image in the database consists of only one MC, so that pixel-wise labels for each image are automatically available. With those homogeneous MCs, multiphase micrographs and their pixel-wise annotations can be generated as described in Section 2.3. This type of generated data has been used as a benchmark to pre-train and evaluate machine learning models related to texture analysis Karabağ et al. (2019); Todorovic and Ahuja (2009); Tivive and Bouzerdoun (2006); Sagiv et al. (2006); Karoui et al. (2006); You and Cohen (1993), and we have found it helpful for pre-training our segmentation/classification models due to the visual similarity of the Brodatz images to many material micrographs.

To perform unsupervised segmentation for this Brodatz data set, we use a linear regression model as the supervised learning model to predict individual pixel grayscale levels, for which the score vectors are computed. We also used a neural network instead of a linear regression model, but the segmentation results were nearly identical, indicating the approach is relatively robust to choice of supervised learning model (Zhang et al. (2021) also observed this; and we consider a neural network model for the example in Fig. 6b). Then, BGM is applied to the score vectors to segment the image and determine the number of MCs, which is illustrated in Fig. 5. Fig. 5a shows an example micrograph and Fig. 5b shows the segmentation results overlaid on the micrograph for the BGM model with 3 segments, which is the true number of HRs in the micrograph. The BGM method has two built-in mechanisms for determining the number of segments. One can conservatively

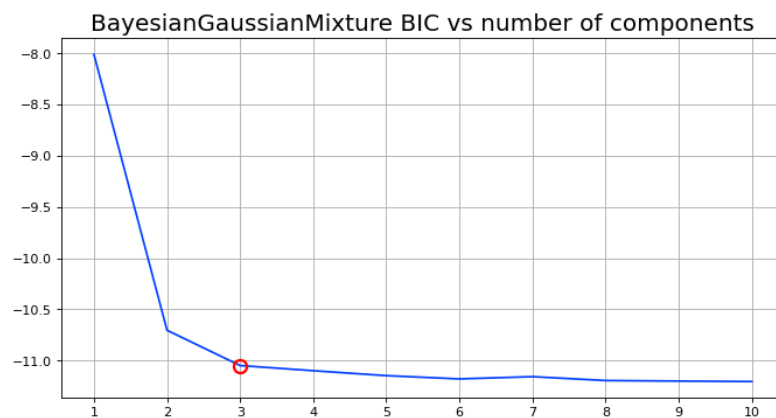


(a) The original micrograph.

(b) Unsupervised segmentation with correct number of MCs.



(c) Posterior weights of segments in BGM applied to the original micrograph.



(d) BIC plot for BGM applied to the original micrograph.

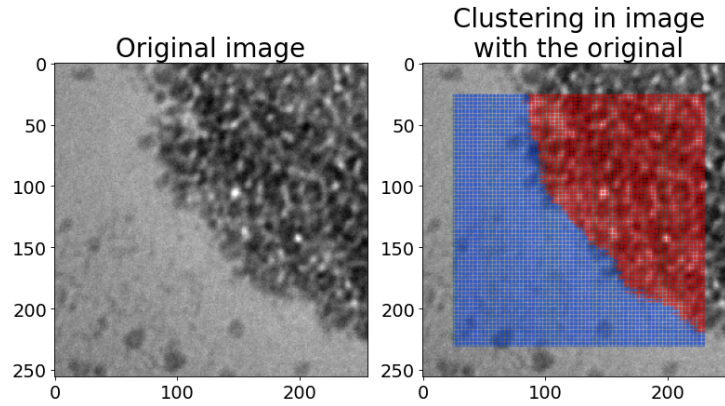
Figure 5: Results of the BMG method of Step 1 applied to the Brodatz data set. (a) A three-phase micrograph, created from the Brodatz data. (b) Unsupervised segmentation results for the micrograph. (c) BGM posterior weights when six clusters are used in the model, indicating that the number of HRs is 3 (since only 3 segments have substantial weights). (d) BIC plot for the BGM model with number of clusters varying from 1 to 10, which also indicates that the number of HRs is 3 (the elbow in the plot is at 3, beyond which the BIC decreases more slowly). The  $\mathcal{AIC}$  generates similar plot.

specify the number of segments and then select the appropriate number of segments as the number of significant posterior weights (the BGM model assigns a posterior weight to each segment, which indicates the extent to which that segment is present). This is illustrated in Fig. 5c for the BGM model with 6 segments. Alternatively, one can plot BIC/AIC for the BGM versus the number of BGM segments and then select the number of segments to coincide with the “elbow” in the plot, after which the BIC/AIC criterion decreases only gradually, which is illustrated in Fig. 5d for BIC (AIC plot is similar). Figs. 5c and 5d both correctly indicate the number of segments is 3 for this example.

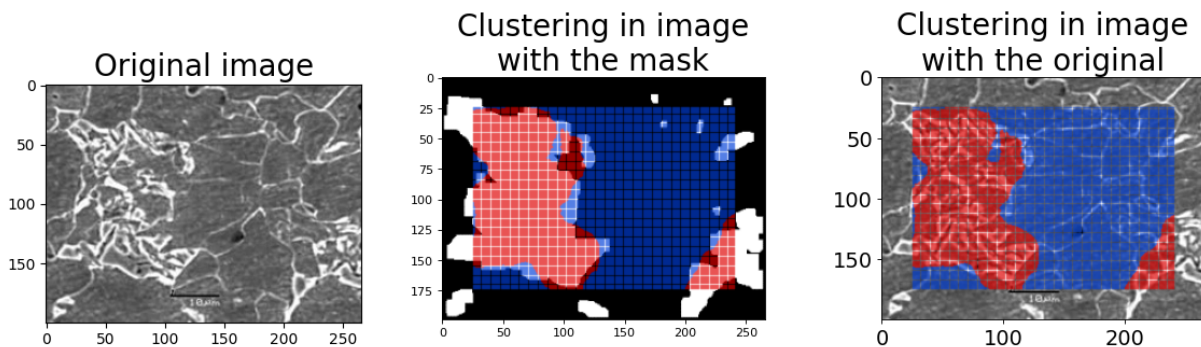
The second data set consists of TEM images of silica particles in PMMA with octyl functional modification (Fig. 1e). Sometimes the particle dispersion is nonstationary across samples or the particles form large agglomerations within one sample, which can affect the physical properties of the materials (e.g., the breakdown stress or dielectric constant Dang et al. (2012)). Fig. 6a shows a micrograph with a large agglomeration, and Fig. 6b shows the Step 1 segmentation results, which correctly separate the agglomeration from the matrix region.

The third data set (Fig. 1f and 6b) is an SEM image of dual-phase steel consisting of ferrite matrix and martensite in the form of islands. Segmenting the two phases is challenging because the ferrite and martensite phases share some similar features and because the martensite phases are not connected in this micrograph. Fig. 6b also shows our segmentation results, which agree quite closely with the ground truth MC labels. The ground truth for this micrograph was available from Banerjee et al. (2013).





(a) A TEM image of silica-PMMA.



(b) An SEM image of a dual-phase steel sample.

Figure 6: The score-based nonstationarity analysis method of Step 1 applied to different microstructure data sets. (a) Segmentation results for a TEM micrograph of silica particles in PMMA with octyl functional modification using a linear regression model as the supervised learner. The left image is the original micrograph while the right one has the segment labels overlapped with the original micrograph. (b) Segmentation results for an SEM micrograph of dual-phase steel using a neural network with 10 hidden layer neurons. The left image is the original micrograph. The middle and the right images are the segment labels from our method overlapped the ground truth mask and the original micrograph respectively, both of which come from Banerjee et al. (2013). In both (a) and (b), we used parameters  $l_s = 5$ ,  $l_w = 20$ .

### 3.2 Step 2: MC Classification and ranking of predicted MCs using a CNN on Kylberg data set

Here we use the Kylberg Kylberg (2011) data set shown in Fig.7, which contains grayscale images of 28 different MCs that are of sufficiently high quality<sup>1</sup> to allow training an accurate classification model. In the Kylberg data, for each of the 28 MCs, 4 images were taken at different positions on a sample, and each of these images are subsequently divided into 40 non-overlapping patches of size  $576 \times 576$  pixels Kylberg (2011). Each patch has 12 rotated versions with in-plane rotation angles varying from 0 to 360 in 30 degree increments. This augmentation increases the sample size to 53,760 with 1,920 image patches for each MC.

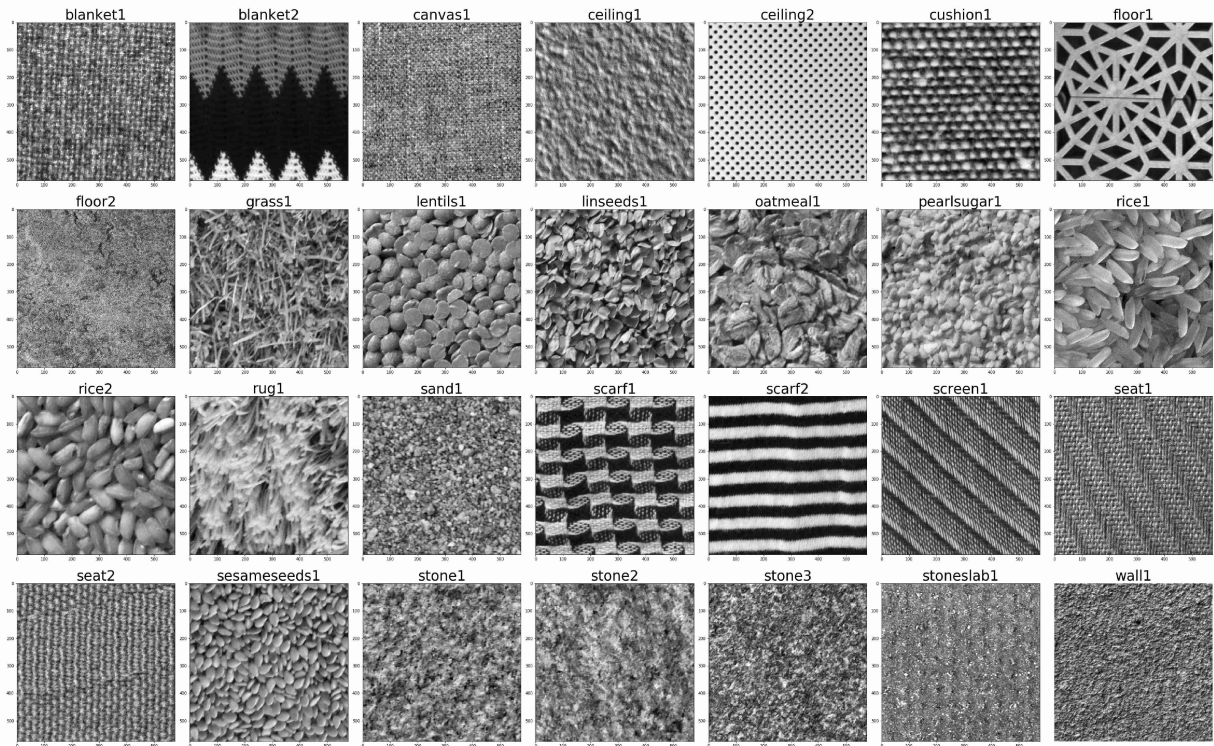


Figure 7: All micrographs in the Kylberg data set with their true label names on top of images that are used to train AlexNet classification network.

<sup>1</sup>Those images are all taken under the same lighting, direction, and distance conditions.

We use 80%, 10%, and 10% of the data for training, validation, and testing, respectively. Images are in grayscale with 256 levels and are not normalized (normalizing the range of pixels), but the mean values of channels from the ILSVRC data set Russakovsky et al. (2015) are subtracted from the images, according to the pre-processing procedure of pre-training AlexNet with the ILSVRC data set<sup>2</sup>. The Adam optimizer Kingma and Ba (2014) is used with default hyper-parameters.

Training such a network from scratch on a new data set of micrographs is time-consuming, especially when the number of MCs is large. Transfer learning techniques can significantly accelerate the training process, even though the pre-trained weights are based on the ILSVRC data set, which contains approximately 1.2 million images representing 1000 object categories, none of which includes microstructures DeCost et al. (2017a) of materials. The benefit of pre-training is evident from Fig. 8, which shows the training and validation loss, accuracy, and top-5 accuracy with and without pre-training. With or without pre-training the validation accuracy and top-5 accuracy both converge to close to 100%, although the pre-trained version reaches high accuracy much faster.

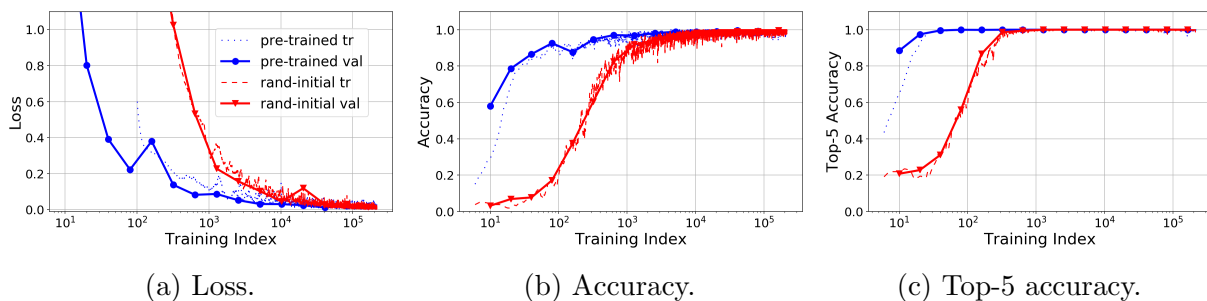


Figure 8: Training and validation metrics for the Step 2 classification and ranking for the Kylberg data set demonstrating the substantial benefit of pre-training.

To demonstrate the effectiveness of the EDL uncertainty quantification for identifying

<sup>2</sup>[http://www.cs.toronto.edu/~guerzhoy/tf\\_alexnet/](http://www.cs.toronto.edu/~guerzhoy/tf_alexnet/)

new MCs not in the existing database in Step 2, we held out 4 of the 28 MCs to serve as new ones. The validation accuracy and top-5 accuracy for the model trained on the micrographs for the 24 included MCs were 98.48% and 100%, respectively. The average EDL uncertainty for the validation data (which contained only the 24 existing MCs) was 24.58%. In contrast, when the model was used to classify the micrographs for the 4 new MCs, the average EDL uncertainty increased to 61.25%, which indicates that the EDL uncertainty can be effectively used to flag new MCs.

### 3.3 Step 3: Segmentation using DeepLabv3+ on Brodatz and materials data sets

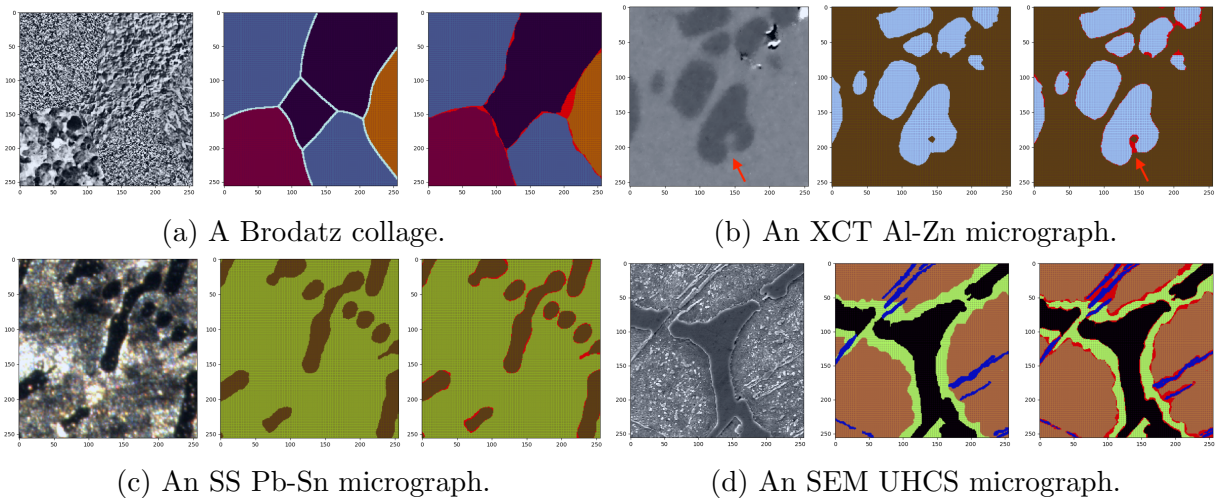


Figure 9: Test results for the Step 3 supervised segmentation of the Brodatz and real materials data sets. For each subfigure, the left image is the micrograph to be segmented; the middle image is the mask showing the ground truth coded with different colors for different MCs (the boundaries between patches in (a) are colored differently); the right image is the predicted labels, with the same color scheme with red indicating misclassified pixels. (a) 4 MCs are different colors. (b) Al and Zn MCs are brown and light blue, respectively. (c) Pb and Sn MCs are green and brown, respectively. (d) ferritic, proeutectoid, spheroidite, and Widmanstätten MCs are green, black, brown, and blue, respectively.

We applied the supervised segmentation to four data sets: Brodatz, two dendrite growth data sets (one a Al-Zn alloy with X-ray computed tomography micrographs (Fig. 1c or 9b) and the other a Pb-Sn alloy with serial sectioning microscopy micrographs (Fig. 1d or 9c)) Stan et al. (2020), and UHCS (Fig. 1a, 1b, or 9d). We train a segmentation model for each data set. The Brodatz data set is generated according to the data-augmentation process described in Section 2.3. Because pixel-wise annotations are obtained automatically, collages of 5 MCs with random and arbitrary boundaries are generated along with labels of MCs as ground truth. The collages as well as boundaries between different HRs are randomly generated for training, validation, and testing data splits so that they are not the same across different data splits. The sample sizes of augmented training, validation, and testing data splits are 20,000, 5,000, and 10,000, respectively. For other real materials data sets, only rotation and flipping are used to augment the data splits. The Al-Zn alloy data set contains 42 original micrographs with resolution  $852 \times 852$ . Smaller micrograph patches of size  $256 \times 256$  are generated from each original micrograph to meet the input dimension of the reduced-size segmentation network described in Section 2.3. The training, validation, and testing data splits are generated from 30, 10, and 2 original micrographs through this patch-generation process, respectively. The sample sizes of augmented training, validation, and testing data splits are 150,000, 21,000, and 10,500, respectively. The Pb-Sn alloy data set contains 9 original micrographs with resolution  $1689 \times 985$ . The training, validation, and testing data splits are generated from 6, 2, and 1 original micrographs using the same patch-generation process. The sample sizes of augmented training, validation, and testing data splits are 370,000, 36,000, and 14,000, respectively. The UHCS

data set contains 24 original micrographs as described in DeCost et al. (2019), each with the resolution  $645 \times 522$  but with different scale bars. For this data set, we evaluate the cross-validation accuracy with each fold generated by a group of 4 original micrographs (in total, we have 6 such groups) through the same patch-generation process. The augmented sample sizes of a training split and a validation fold are 140,000 and 3,500, respectively, and we cycle through all 6 folds. Because each micrograph is at a different scale, we rescaled all micrographs so that pixels correspond to the same physical length.

As seen in the right plots of the subfigures in Fig. 9, the predicted MC labels for the test cases agree quite closely with the true labels in the middle plots, and only a small portion of pixels near the boundary regions are mis-segmented (boundaries are obviously more difficult to classify and sometimes ambiguous in real micrographs). For the Brodatz data set in Fig. 9a, the overall (pixel-wise) test accuracy is 97.8% with all MCs having true positive rates larger than 96%; for the Al-Zn micrographs in Fig. 9b the overall test accuracy is 99.51%, and the true positive rate for the Al and Zn are 99.41% and 99.61%; for Pb-Sn micrographs, the overall test accuracy is 97.58%, and the true positive rate for Pb and Sn are 97.83% and 96.70%; for UHCS micrographs in Fig. 9d, the overall test accuracy is 93.1%, and the true positive rate for ferritic, proeutectoid, spheroidite, and Widmanstätten are 90.7%, 94.2%, 95.1%, and 89.6% respectively.

In addition to achieving high accuracy, our supervised segmentation network has other desirable features. One issue often encountered in real applications is that the scale of micrographs may differ from sample to sample. For example, different SEM images of the same microstructure may have somewhat different magnifications. To test the impact of

small scaling variations on micrograph segmentation, for each patch in a collage we randomly choose the scale of MCs to lie within the interval  $[1, 1.1]$ , enlarge them accordingly, and then crop and paste all patches together. Our experiments show that the test accuracy (loss) are approximately the same as without scaling. This is likely because the ASPP layer in DeepLabv3+ extracts multi-scale patterns in one layer and thus is robust to such small changes in scaling.

Segmenting real micrographs can be challenging because of some ambiguity in true labels. As in Fig. 9b, there is a small island of class 1 (Al) in one branch of the dendrites (the red arrows) and the algorithm correctly captures that, even though it misclassifies a bridge that connects the island and the rest of the bulk Al. From the original image, the misclassified part has much lighter intensity than other parts of class 2 (Zn), which is likely the reason our algorithm misclassified it.

We also found that transfer learning accelerates the training of the Step 3 models, similar to what we described under Step 2 (Fig. 8). In particular, we found that pre-training on the Brodatz data before training on real material data substantially accelerated the training, relative to using random initial weights when training on the real data (results omitted for brevity), in spite of the Brodatz data having its own stochastic nature that may or may not be similar to real material micrographs.

### 3.4 Iteration over Steps 1-3: Iteratively characterizing new samples on Brodatz data set

We now use the Brodatz data set to simulate the scenario where Steps 1-3 are iteratively repeated to identify new MCs and integrate them into the database, because the number of MCs is easily controlled. We begin with 4 MCs and increase their number by one at each iteration until the database contains 22 MCs.

In Sec. 3.2 and 3.3, transfer learning was helpful for accelerating model training. Here, we demonstrate that it is also helpful when retraining the models at each iteration of Steps 1-3. Suppose that a supervised segmentation model in Step 3, denoted by  $\mathcal{M}_k$ , has been trained on a database with  $k$  MCs. The naive approach of training the supervised segmentation model when the  $(k + 1)^{\text{st}}$  MC is added is to retrain the model  $\mathcal{M}_{k+1}$  with all weights randomly initialized. Alternatively, we can retain the parameters in the trained  $\mathcal{M}_k$ , expand the number of channels in the last layer to classify  $k + 1$  classes, randomly initialize only those newly added weights associated with the channel corresponding to the  $(k + 1)^{\text{st}}$  MC, and continue training the network with old and new samples. As seen in Fig. 10, as the number of classes increases, the transfer learning is consistently better than complete retraining method and achieves very high accuracy when new MCs are added, as well as faster convergence.



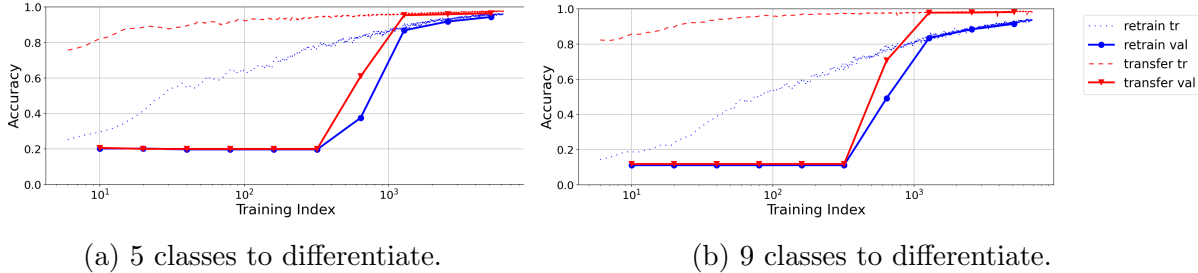


Figure 10: Training (tr) and validation (val) accuracy for two ways of training when iterating over Steps 1-3 (results shown at iterations  $k = 5$  and  $k = 9$ ): Complete retraining with all weights randomly initialized (“retrain”), transfer learning with only the weights of the new channel associated with the new MC randomly initialized, followed by training the entire network (“transfer”).

## 4 Conclusions

This study integrates unsupervised segmentation, supervised uncertainty-aware classification, and supervised segmentation to provide a comprehensive framework characterizing microstructures of multiphase materials, an increasingly important goal in materials science. This framework is designed for iterative use, with each iteration characterizing and segmenting multiphase materials and integrating newly identified MCs into a database, improving the characterization performance at each iteration. We have demonstrated the performance of each procedural step on a variety of real and synthetic micrograph examples and also demonstrated the ability to identify new MCs (through evidential deep learning) and incorporate them into the database to facilitate the characterization of a broader range of materials. We have also shown that data augmentation and transfer learning techniques can be used to enhance the performance of the framework. One limitation of the framework is that it is designed to characterize microstructures having stochastic behavior. For microstructures with more structured geometric patterns, further investigation is needed.

## Acknowledgement

This research work was partially supported by the Air Force Office of Scientific Research under grants FA9550-14-1-0032 and FA9550-18-1-0381, for which we express our sincere gratitude. Additionally, this work was also supported by funded resources from the Extreme Science and Engineering Discovery Environment (XSEDE) Towns et al. (2014) (NSF grant ACI-1548562) and the Advanced Cyberinfrastructure Coordination Ecosystem: Services & Support (ACCESS) program Boerner et al. (2023) (NSF grants 2138259, 2138286, 2138307, 2137603, and 2138296). Further computational resources were provided by the Quest high-performance computing facility at Northwestern University, which is jointly supported by the Office of the Provost, the Office for Research, and Northwestern University Information Technology. The micrographs of silica particles in PMMA are kindly provided by Prof. Linda Schadler (Linda.Schadler@uvm.edu).

## References

- AFRL (2018), “AFRL (2018) Air Force Research Laboratory (AFRL) additive manufacturing (AM) modeling challenge series.”.
- Agrawal, Ankit and Choudhary, Alok (2016), “Perspective: Materials informatics and big data: Realization of the “fourth paradigm” of science in materials science,” *Appl Materials*, 4, 5, 053208.
- (2019), “Deep materials informatics: Applications of deep learning in materials science,” *MRS Communications*, 9, 3, 779–792.

- Ajioka, Fumito, Wang, Zhi-Lei, Ogawa, Toshio, and Adachi, Yoshitaka (2020), “Development of High Accuracy Segmentation Model for Microstructure of Steel by Deep Learning,” *ISIJ International*, ISIJINT–2019.
- Ashby, Michael F and Cebon, D (1993), “Materials selection in mechanical design,” *Le Journal de Physique IV*, 3, C7, C7–1.
- Azimi, Seyed Majid, Britz, Dominik, Engstler, Michael, Fritz, Mario, and Mücklich, Frank (2018), “Advanced steel microstructural classification by deep learning methods,” *Scientific reports*, 8, 1, 1–14.
- Balla, Vamsi Krishna, Bhat, Abhimanyu, Bose, Susmita, and Bandyopadhyay, Amit (2012), “Laser processed TiN reinforced Ti6Al4V composite coatings,” *Journal of the mechanical behavior of biomedical materials*, 6, 9–20.
- Bandyopadhyay, Amit and Heer, Bryan (2018), “Additive manufacturing of multi-material structures,” *Materials Science and Engineering: R: Reports*, 129, 1–16.
- Banerjee, Siddhartha, Ghosh, Swarup Kumar, Datta, Shubhabrata, and Saha, Sanjoy Kumar (2013), “Segmentation of dual phase steel micrograph: An automated approach,” *Measurement*, 46, 8, 2435–2440.
- Bishop, Christopher M (2006), “Pattern recognition and machine learning,” *Springer google schola*, 2, 1122–1128.
- Blaiszik, Ben, Chard, Kyle, Pruyne, Jim, Ananthakrishnan, Rachana, Tuecke, Steven, and

- Foster, Ian (2016), “The Materials Data Facility: Data services to advance materials science research,” *JOM*, 68, 8, 2045–2052.
- Blei, David M, Ng, Andrew Y, and Jordan, Michael I (2003), “Latent dirichlet allocation,” *Journal of machine Learning research*, 3, Jan, 993–1022.
- Boerner, Timothy J, Deems, Stephen, Furlani, Thomas R, Knuth, Shelley L, and Towns, John (2023), “Access: Advancing innovation: Nsf’s advanced cyberinfrastructure coordination ecosystem: Services & support,” In *Practice and Experience in Advanced Research Computing*, ed. I. *Practice and Experience in Advanced Research Computing*, pp. 173–176.
- Bostanabad, Ramin, Bui, Anh Tuan, Xie, Wei, Apley, Daniel W, and Chen, Wei (2016), “Stochastic microstructure characterization and reconstruction via supervised learning,” *Acta Materialia*, 103, 89–102.
- Brodatz, Phil (1966), *Textures: a photographic album for artists and designers*, Dover Pubns.
- Bui, Anh Tuan and Apley, Daniel W (2018), “Monitoring for changes in the nature of stochastic textured surfaces,” *Journal of Quality Technology*, 50, 4, 363–378.
- Carter, Luke N, Martin, Christopher, Withers, Philip J, and Attallah, Moataz M (2014), “The influence of the laser scan strategy on grain structure and cracking behaviour in SLM powder-bed fabricated nickel superalloy,” *Journal of Alloys and Compounds*, 615, 338–347.

- Chen, Dali, Zhang, Pengyuan, Liu, Shixin, Chen, Yangquan, and Zhao, Wei (2019a), “Aluminum alloy microstructural segmentation in micrograph with hierarchical parameter transfer learning methoda,” *Journal of Electronic Imaginga*, 28, 5, 053018.
- Chen, Liang-Chieh, Papandreou, George, Kokkinos, Iasonas, Murphy, Kevin, and Yuille, Alan L (2017), “Deeplab: Semantic image segmentation with deep convolutional nets, atrous convolution, and fully connected crfs,” *IEEE transactions on pattern analysis and machine intelligence*, 40, 4, 834–848.
- Chen, Liang-Chieh, Zhu, Yukun, Papandreou, George, Schroff, Florian, and Adam, Hartwig (2018),, Encoder-decoder with atrous separable convolution for semantic image segmentation. in *Proceedings of the European conference on computer vision (ECCV)*, 801–818.
- Chen, Zhangwei, Li, Ziyong, Li, Junjie, Liu, Chengbo, Lao, Changshi, Fu, Yuelong, Liu, Changyong, Li, Yang, Wang, Pei, and He, Yi (2019b), “3D printing of ceramics: A reviewb,” *Journal of the European Ceramic Societyb*, 39, 4, 661–687.
- Chollet, François (2017),, Xception: Deep learning with depthwise separable convolutions. in *Proceedings of the IEEE conference on computer vision and pattern recognition*, 1251–1258.
- Dang, Zhi-Min, Yuan, Jin-Kai, Zha, Jun-Wei, Zhou, Tao, Li, Sheng-Tao, and Hu, Guo-Hua (2012), “Fundamentals, processes and applications of high-permittivity polymer–matrix composites,” *Progress in materials science*, 57, 4, 660–723.
- DeCost, Brian L, Francis, Toby, and Holm, Elizabeth A (2017a), “Exploring the mi-

crostructure manifold: image texture representations applied to ultrahigh carbon steel microstructuresa,” *Acta Materialia*, 133, 30–40.

DeCost, Brian L, Hecht, Matthew D, Francis, Toby, Webler, Bryan A, Picard, Yoosuf N, and Holm, Elizabeth A (2017b), “UHCSDB: UltraHigh carbon steel micrograph database,” *Integrating Materials and Manufacturing Innovation*, 6, 2, 197–205.

DeCost, Brian L and Holm, Elizabeth A (2015), “A computer vision approach for automated analysis and classification of microstructural image data,” *Computational materials science*, 110, 126–133.

DeCost, Brian L, Lei, Bo, Francis, Toby, and Holm, Elizabeth A (2019), “High throughput quantitative metallography for complex microstructures using deep learning: a case study in ultrahigh carbon steel,” *Microscopy and Microanalysis*, 25, 1, 21–29.

Efros, Alexei A and Leung, Thomas K (1999),, Texture synthesis by non-parametric sampling. in *Proceedings of the seventh IEEE international conference on computer vision*, vol. 2, 1033–1038. IEEE.

Gagliardi, Dimitri (2015), “Material data matter—Standard data format for engineering materials,” *Technological Forecasting and Social Change*, 101, 357–365.

Hecht, Matthew D, Webler, Bryan A, and Picard, Yoosuf N (2016), “Digital image analysis to quantify carbide networks in ultrahigh carbon steels,” *Materials Characterization*, 117, 134–143.

Huang, Shih-Cheng, Pareek, Anuj, Jensen, Malte, Lungren, Matthew P, Yeung, Serena, and

- Chaudhari, Akshay S (2023), “Self-supervised learning for medical image classification: a systematic review and implementation guidelines,” *NPJ Digital Medicine*, 6, 1, 74.
- Impoco, Gaetano and Tuminello, L (2015), “Incremental learning to segment micrographs,” *Computer Vision and Image Understanding*, 140, 144–152.
- Jain, Anubhav, Hautier, Geoffroy, Ong, Shyue Ping, and Persson, Kristin (2016a), “New opportunities for materials informatics: resources and data mining techniques for uncovering hidden relationships,” *Journal of Materials Research*, 31, 8, 977–994.
- Jain, Anubhav, Persson, Kristin A, and Ceder, Gerbrand (2016b), “Research Update: The materials genome initiative: Data sharing and the impact of collaborative ab initio databases,” *APL Materials*, 4, 5, 053102.
- Jang, Junmyoung, Van, Donghyun, Jang, Hyojin, Baik, Dae Hyun, Yoo, Sang Duk, Park, Jaewoong, Mhin, Sungwook, Mazumder, Jyoti, and Lee, Seung Hwan (2019), “Residual neural network-based fully convolutional network for microstructure segmentation,” *Science and Technology of Welding and Joining*, 1–8.
- Karabağ, Cefa, Verhoeven, Jo, Miller, Naomi Rachel, and Reyes-Aldasoro, Constantino Carlos (2019), “Texture Segmentation: An Objective Comparison between Five Traditional Algorithms and a Deep-Learning U-Net Architecture,” *Applied Sciences*, 9, 18, 3900.
- Karoui, Imen, Fablet, Ronan, Boucher, J-M, and Augustin, J-M (2006), “Region-based image segmentation using texture statistics and level-set methods. in *2006 IEEE Inter-*

*national Conference on Acoustics Speech and Signal Processing Proceedings*, vol. 2, II–II. IEEE.

Kim, Chiho, Pilania, Ghanshyam, and Ramprasad, Ramamurthy (2016), “From organized high-throughput data to phenomenological theory using machine learning: the example of dielectric breakdown,” *Chemistry of Materials*, 28, 5, 1304–1311.

Kingma, Diederik P and Ba, Jimmy (2014), “Adam: A method for stochastic optimization,” *arXiv preprint arXiv:1412.6980*.

Kitahara, Andrew R and Holm, Elizabeth A (2018), “Microstructure Cluster Analysis with Transfer Learning and Unsupervised Learning,” *Integrating Materials and Manufacturing Innovation*, 7, 3, 148–156.

Kondo, Ruho, Yamakawa, Shunsuke, Masuoka, Yumi, Tajima, Shin, and Asahi, Ryoji (2017), “Microstructure recognition using convolutional neural networks for prediction of ionic conductivity in ceramics,” *Acta Materialia*, 141, 29–38.

Kotz, Samuel, Balakrishnan, Narayanaswamy, and Johnson, Norman L (2019), *Continuous multivariate distributions, Volume 1: Models and applications*, vol. 334, John Wiley & Sons.

Krizhevsky, Alex, Sutskever, Ilya, and Hinton, Geoffrey E (2012),, Imagenet classification with deep convolutional neural networks. in *Advances in neural information processing systems*, 1097–1105.



- Kylberg, Gustaf (2011), *Kylberg Texture Dataset v. 1.0*, Centre for Image Analysis, Swedish University of Agricultural Sciences and . . . .
- Lewandowski, John J and Seifi, Mohsen (2016), “Metal additive manufacturing: a review of mechanical properties,” *Annual Review of Materials Research*, 46, 151–186.
- Ligon, Samuel Clark, Liska, Robert, Stampfl, Jürgen, Gurr, Matthias, and Mühlaupt, Rolf (2017), “Polymers for 3D printing and customized additive manufacturing,” *Chemical reviews*, 117, 15, 10212–10290.
- Liu, Zelong, Kainth, Komal, Zhou, Alexander, Deyer, Timothy W, Fayad, Zahi A, Greenspan, Hayit, and Mei, Xueyan (2024), “A review of self-supervised, generative, and few-shot deep learning methods for data-limited magnetic resonance imaging segmentation,” *NMR in Biomedicine*, e5143.
- Long, Jonathan, Shelhamer, Evan, and Darrell, Trevor (2015), Fully convolutional networks for semantic segmentation. in *Proceedings of the IEEE conference on computer vision and pattern recognition*, 3431–3440.
- Lubbers, Nicholas, Lookman, Turab, and Barros, Kipton (2017), “Inferring low-dimensional microstructure representations using convolutional neural networks,” *Physical Review E*, 96, 5, 052111.
- Maik Jablonka, Kevin, Ongari, Daniele, Mohamad Moosavi, Seyed, and Smit, Berend (2020), “Big-Data Science in Porous Materials: Materials Genomics and Machine Learning,” *arXiv*, arXiv–2001.

- Michel, Kyle and Meredig, Bryce (2016), “Beyond bulk single crystals: a data format for all materials structure-property-processing relationships,” *Mrs Bulletin*, 41, 8, 617.
- Moritz, Tassilo and Maleksaeedi, Saeed (2018), “Additive manufacturing of ceramic components,” In *Additive Manufacturing*, ed. I. *Additive Manufacturing*, Elsevier, pp. 105–161.
- O’Mara, Jordan, Meredig, Bryce, and Michel, Kyle (2016), “Materials data infrastructure: a case study of the citrination platform to examine data import, storage, and access,” *Jom*, 68, 8, 2031–2034.
- Puchala, Brian, Tarcea, Glenn, Marquis, Emmanuelle A, Hedstrom, Margaret, Jagadish, HV, and Allison, John E (2016), “The materials commons: a collaboration platform and information repository for the global materials community,” *Jom*, 68, 8, 2035–2044.
- Qi, Haozhi, Zhang, Zheng, Xiao, Bin, Hu, Han, Cheng, Bowen, Wei, Yichen, and Dai, Jifeng (2017),, Deformable convolutional networks–coco detection and segmentation challenge 2017 entry. in *ICCV COCO Challenge Workshop*, vol. 15.
- Randen, Trygve and Husoy, John Hakon (1999), “Filtering for texture classification: A comparative study,” *IEEE Transactions on pattern analysis and machine intelligence*, 21, 4, 291–310.
- Ronneberger, Olaf, Fischer, Philipp, and Brox, Thomas (2015),, U-net: Convolutional networks for biomedical image segmentation. in *International Conference on Medical image computing and computer-assisted intervention*, 234–241. Springer.
- Rose, Frisco, Toher, Cormac, Gossett, Eric, Oses, Corey, Nardelli, Marco Buongiorno,

- Fornari, Marco, and Curtarolo, Stefano (2017), “AFLUX: The LUX materials search API for the AFLOW data repositories,” *Computational Materials Science*, 137, 362–370.
- Russakovsky, Olga, Deng, Jia, Su, Hao, Krause, Jonathan, Satheesh, Sanjeev, Ma, Sean, Huang, Zhiheng, Karpathy, Andrej, Khosla, Aditya, Bernstein, Michael, et al. (2015), “Imagenet large scale visual recognition challenge,” *International journal of computer vision*, 115, 3, 211–252.
- Sagiv, Chen, Sochen, Nir A, and Zeevi, Yehoshua Y (2006), “Integrated active contours for texture segmentation,” *IEEE transactions on image processing*, 15, 6, 1633–1646.
- Sensoy, Murat, Kaplan, Lance, and Kandemir, Melih (2018), “Evidential deep learning to quantify classification uncertainty,” *Advances in neural information processing systems*, 31.
- Stan, Tiberiu, Thompson, Zachary T, and Voorhees, Peter W (2020), “Optimizing convolutional neural networks to perform semantic segmentation on large materials imaging datasets: X-ray tomography and serial sectioning,” *Materials Characterization*, 110119.
- Strohmann, Tobias, Bugelnig, Katrin, Breitbarth, Eric, Wilde, Fabian, Steffens, Thomas, Germann, Holger, and Requena, Guillermo (2019), “Semantic segmentation of synchrotron tomography of multiphase Al-Si alloys using a convolutional neural network with a pixel-wise weighted loss function,” *Scientific Reports*, 9, 1, 1–9.
- Takahashi, Keisuke and Tanaka, Yuzuru (2016), “Materials informatics: a journey towards material design and synthesis,” *Dalton Transactions*, 45, 26, 10497–10499.

- Teh, Yee, Jordan, Michael, Beal, Matthew, and Blei, David (2004), “Sharing clusters among related groups: Hierarchical Dirichlet processes,” *Advances in neural information processing systems*, 17.
- Tivive, Fok Hing Chi and Bouzerdoum, Abdesselam (2006),, Texture classification using convolutional neural networks. in *TENCON 2006-2006 IEEE Region 10 Conference*, 1–4. IEEE.
- Todorovic, Sinisa and Ahuja, Narendra (2009),, Texel-based texture segmentation. in *2009 IEEE 12th International Conference on Computer Vision*, 841–848. IEEE.
- Towns, John, Cockerill, Timothy, Dahan, Maytal, Foster, Ian, Gaither, Kelly, Grimshaw, Andrew, Hazlewood, Victor, Lathrop, Scott, Lifka, Dave, Peterson, Gregory D, et al. (2014), “XSEDE: accelerating scientific discovery,” *Computing in science & engineering*, 16, 5, 62–74.
- Xu, Hongyi, Dikin, Dmitriy A, Burkhart, Craig, and Chen, Wei (2014), “Descriptor-based methodology for statistical characterization and 3D reconstruction of microstructural materials,” *Computational Materials Science*, 85, 206–216.
- Xu, Hongyi, Liu, Ruoqian, Choudhary, Alok, and Chen, Wei (2015), “A machine learning-based design representation method for designing heterogeneous microstructures,” *Journal of Mechanical Design*, 137, 5.
- Yabansu, Yuksel C, Steinmetz, Philipp, Hötzer, Johannes, Kalidindi, Surya R, and Nestler, Britta (2017), “Extraction of reduced-order process-structure linkages from phase-field simulations,” *Acta Materialia*, 124, 182–194.

You, Jane and Cohen, Harvey A (1993), “Classification and segmentation of rotated and scaled textured images using texture “tuned” masks,” *Pattern Recognition*, 26, 2, 245–258.

Yu, Shuangcheng, Zhang, Yichi, Wang, Chen, Lee, Won-kyu, Dong, Biqin, Odom, Teri W, Sun, Cheng, and Chen, Wei (2017), “Characterization and design of functional quasi-random nanostructured materials using spectral density function,” *Journal of Mechanical Design*, 139, 7.

Zhang, Dan, Zhou, Fangfang, Albu, Felix, Wei, Yuanzhou, Yang, Xiao, Gu, Yuan, and Li, Qiang (2023), “Unleashing the power of self-supervised image denoising: A comprehensive review,” *arXiv preprint arXiv:2308.00247*.

Zhang, Kungang, Apley, Daniel W, and Chen, Wei (2021), “Nonstationarity Analysis of Materials Microstructures via Fisher Score Vectors,” *Acta Materialia*, 116818.